Depth-profiling of residual stress and microstructure for austenitic stainless steel surface treated by cavitation, shot and laser peening

Document Version
Accepted author manuscript

[Link to publication record in Manchester Research Explorer](#)

Depth-profiling of residual stress and microstructure for austenitic stainless steel surface treated by cavitation, shot and laser peening

Masayoshi Kumagai[a, b], Matthew E. Curd[b], Hitoshi Soyama[c], Támas Ungár[d, e], Gábor Ribárik[e], Philip J. Withers [b]

[a] Department of Mechanical Systems Engineering, Tokyo City University, 1-28-1 Tamazutsumi, Setagaya-Ku, Tokyo, Japan 158-8557

[b] Henry Royce Institute, Department of Materials, The University of Manchester, Manchester, M13 9PL, UK

[c] Department of Finemechanics, Tohoku University, 6-6-01Aramaki-Aoba, Aoba-Ku, Sendai, Japan 980-8579

[d] Department of Materials, The University of Manchester, Manchester, M13 9PL, UK

[e] Department of Materials Physics, Eötvös Loránd University Budapest, H-1518 Budapest, Hungary, PO Box 32

Abstract

While the general characteristics of various peening techniques have been established, there have been few comparative studies. Here we compare the variation of the residual stresses and microstructural characteristics with depth for 316L austenitic stainless steel treated by cavitation peening (CP), shot peening (SP) and laser peening (LP) all peened to similar intensity levels. While the plastically affected depths were similar in all cases (~400 μm), the SP specimen showed the most extensive near surface plastic deformation, deformation twinning, dislocation density and compressive residual stress. To counterbalance this, the compressive residual stresses extended deeper for the LP and CP. Across the three treatments, a similar dependency was found between diffraction peak broadening and hardness. The dislocation density at the surface determined by the diffraction line profile analysis (LPA) for the SP specimen (4.9×10^{15} m^{-2}) was approximately 2.5 times that for the CP and LP specimens (2.0×10^{15} and 2.1×10^{15} m^{-2}). Electron backscatter diffraction (EBSD) shows that the extensive work introduced by the SP had generated planar defects near to the surface. The increase in yield stress estimated from the hardness corresponded with the increase in dislocation density obtained by the LPA.

Keywords: stress/strain measurements, X-ray analysis, iron alloys, hardness, work hardening, surface treatment

1. Introduction

Peening is used to introduce compressive residual stresses and microstructurally alter and harden the near-surface region of many components. This has been shown to have significant benefits in terms of

performance. For example, in many cases peening treatments have been found to increase the fatigue limit and number of cycles to failure [1–5]. The peening treatment not only modifies the near surface stress state, but also alters the mechanical properties and local microstructure due to the plastic deformation that is introduced [6–8]. After crack formation the near surface stress and microstructure changes can also affect the crack growth rate [9–11]. In addition, the associated increase in hardness can also improve the wear resistance [12,13]. The corrosion resistance has been reported to be affected by the residual stress [14,15] which means that peening can also be effective in suppressing stress corrosion cracking [2,16–18].

There are many different ways to peen a surface. Shot-peening (SP) is most commonly used, being deployed across numerous applications [19–25], e.g. coil springs for automotive [19]. Over the last two decades, laser-peening (LP) and cavitation-peening (CP) have been proposed and are finding increasing application [26–32]. Since each peening method modifies the surface in a different way and to different depths, it is critical to select the most appropriate treatment depending on the particular requirements. However, while the general characteristics of different peening techniques have been established, few comparative studies of the effects have been published [5,33–35] and most of these do not compare the treatments at similar peening intensities making proper comparisons difficult. Therefore, in order to understand the characteristic features of each peening technique a direct comparison is required. This is important if the most appropriate peening method is to be selected, rather than simply selecting the best peening conditions for a given treatment method for a given application. For these purposes, it is important to evaluate the stress state and surface microstructure for each peening method as a function of depth from the surface.

In this study, various measurements on the surface and subsurface were performed to characterise the near surface modified zone for shot, laser and cavitation peening. To better understand the near surface changes in microstructure and residual stress introduced by the peening methods, we examine specimens peened to similar intensities. In each case the residual stress is depth profiled, the surface hardness quantified and the microstructure evaluated by electron backscatter diffraction (EBSD). In addition, diffraction line profile analysis (LPA) is used for quantitative characterisation of lattice defect densities.

2. Experimental

2.1 Specimen

Austenitic stainless steel (JIS SUS316L) was used for the peening experiments. The 0.2% proof stress, tensile strength, and elongation of this steel are 308 MPa, 572 MPa, and 53%, respectively. The CP, SP, and LP were performed on one side of 6 mm thick plate-shaped samples, with the dimensions 200 × 50 mm^2 for the CP, 120 × 30 mm^2 for the SP, and 30 × 30 mm^2 for the LP. Additionally, an unpeened specimen, was prepared to act as a reference. To facilitate a comparison of the different methods, each

peening condition was selected to achieve a similar level of curvature along the longitudinal direction of the sample. The processing times were four times that needed to induce curvature of 1.4 m^{-1}. The set up for the CP is described in more detail elsewhere [35]; in essence, a water jet was applied at a pressure of 30 MPa with a flow rate of 3×10^{-2} m^3/min. The cavitation number was 0.0033, and the standoff distance was 222 mm [5,35,36]. The number of scans was 20 with a scanning speed of 1 mm/s. For the SP, spherical SUS440C shot media having a 3.2 mm diameter were used [5]. The shots were bombarded using a water jet system (see [37]). The processing rate was 0.667 s/mm. The submerged laser peening method was used without a coating [38]. The LP was performed using a Q-switched Nd: YAG laser having a wavelength of 1064 nm, pulse energy of 0.35 J, pulse width of 6 ns, and frequency of 10 Hz. The diameter of the beam spot size on the work surface was 0.8 mm[5]. The pulse density was 20 pulses/mm^2.

2.2 X-ray stress measurement

For the stress measurements, the CP and SP samples were cut into five and three pieces respectively to give 50×40 mm^2 and 30×40 mm^2 coupons; comparable in size to the LP samples. In each case, one piece was used for the residual stress depth profiling using an X-ray stress measurement system with two detectors (iXRD, PROTO). Mn-Kα characteristic X-rays without Kβ filter and their γFe311 reflections were used for the measurement. The stresses were obtained using the $\sin^2\psi$ method [39,40]. The stress constant was −303 MPa/deg. Depth-profiles were obtained by incremental layer removal through repeated cycles of electropolishing and stress measurements. The electropolishing was performed with a solution of 10% perchloric acid and 90% methanol on a partial circular area, approximately 10 mm in diameter. Finer polishing steps (~10 μm) were used closer to the peened surface than in the deeper regions. However, the depth of material removed by electropolishing cannot be controlled precisely, and as such the polishing steps vary somewhat (see Fig.1). The depth of material removed by each polishing step was recorded using a micrometer.

2. 3 Surface profilometry, hardness testing, and EBSD analysis

The surface topographies arising from the surface treatments were mapped by a laser confocal microscope (VK-X200, Keyence). In order to observe a large area, four maps were collected using the x20 objective lens and merged to form a composite map.

For depth-profiling of the hardness, nanoindentation was performed on the cross-section of each specimen. After cutting the specimen perpendicular to the peened surface, the cross-sections were polished using SiC grinding paper (up to P4000), diamond paste (3, 1 and 0.25 μm), and colloidal silica solution. The hardness variation was measured using a nanoindentation tester (Nano Indenter XP, MTST), operating with an indentation depth of 1000 nm, a strain rate of 0.05 s^{-1} and a peak hold time of 10 s. Vickers hardness tests were also performed in the matrix (the deeper regions) of the three

samples by a Matsuzawa MMT-X7A indenter for the general benchmark. For this test, the load was 9.81 N (100 gf), and the holding duration was 10 s.

To identify the microstructures beneath the peened surface, EBSD analysis was performed on the cross-sections, which were first re-prepared using the same grinding and polishing method as for the nanoindentation tests. EBSD was conducted on a FEI Magellan 400 scanning electron microscope equipped with a Nordlys EBSD detector, running Aztec (Oxford Inst.) acquisition software. For each map, patterns were obtained using a beam energy of 15 keV, beam current of 1.6 nA, step size of 0.1 μm and 4x4 detector binning.

2.4 X-ray diffraction line profile analysis

In order to characterise the dislocation density, X-ray diffraction line profile analysis was performed. The line profiles for each specimen were measured using an X-ray diffractometer (SmartLab, Rigaku) with Bragg–Brentano geometry and a 1-D detector. The Kα line from a copper target was used, with a Nickel filter to eliminate the K_β line. The scanning conditions were chosen such that the peak height from the background of each reflection was approximately 10,000 counts in the diffraction angle (2θ) between 38 to 145°. 400 reflections were eliminated due to their weak intensities. Lanthanum hexaboride powder (SRM660c, NIST) was used as a standard specimen to deconvolute peak broadening from instrumental factors. The CMWP software [41,42] was used for the line profile analysis. The lattice constant is 0.36469 nm [43], and the Burgers vector on <110>{111} is 0.25788 nm in length. The averaged contrast factor for the $h00$ reflection was 0.297, which was obtained via ANIZIC [44] with the elastic stiffness [45].

3. Results

3.1 Residual stress depth-profiles

Fig.1 shows the variation of the in-plane stresses and full-width at half-maximum (FWHM) of X-ray diffraction as a function of depth for the 3 surface treatments. Each value of FWHM was the average of FWHMs at all $\sin^2\psi$ on one of the detectors. On the CP and SP specimens, the residual stresses in x and y directions agreed at every depth. On the other hand, in the LP specimen, the residual stresses differed notably at small depths. Anisotropic stresses have been reported previously and explained due to unidirectional processing[16]. The FWHM values along the two directions were similar in all specimens suggesting an absence of in-plane microstructural anisotropy.
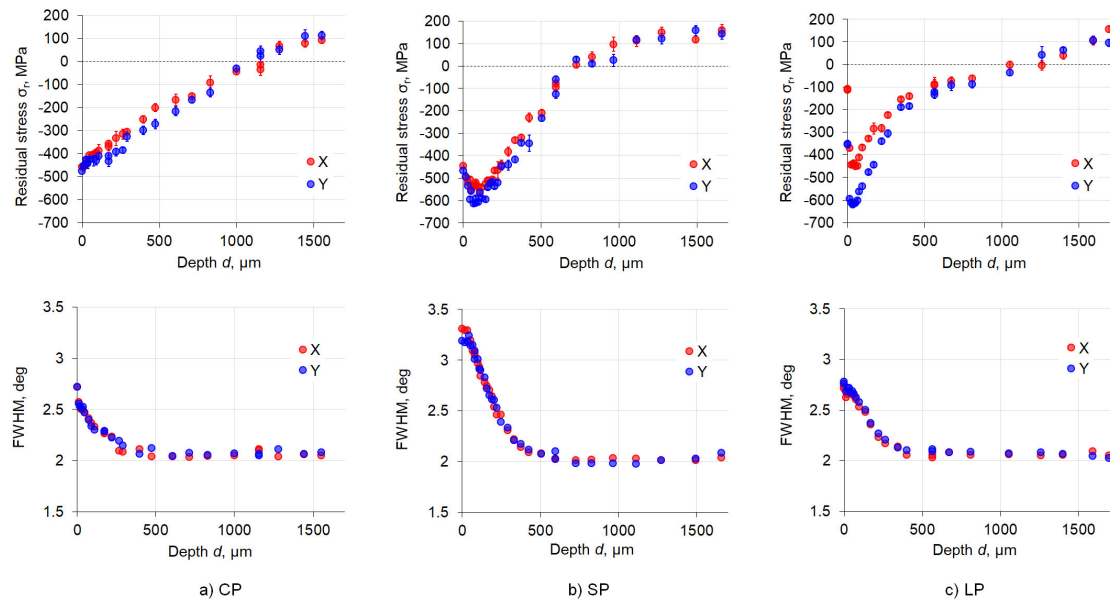
Fig. 1. *In-plane residual stress (top) and FWHM depth-profiles (bottom) recorded in the x and y directions for a) CP, b) SP and c) LP by X-ray diffraction using γFe 311 reflections.*

The residual stress depth-profiles for each treatment are compared alongside that for the unpeened sample in Fig.2. The residual stresses for the unpeened specimen are small at all depths (average of 12 ± 7 MPa). For the CP treatment, the residual stress is largest (-470 MPa) at the surface and decreases monotonically reaching zero at a depth of around 1200 μm. By contrast, the peak compressive stresses on the SP and LP specimens are located subsurface (100 μm and 50 μm beneath the surface respectively). In comparing these profiles, it is important to remember that the treatments were applied to give approximately the same extent of specimen curvature. Although the surface stresses for the SP and LP specimens are -455 MPa and -230 MPa respectively, the peak stresses of -575 MPa and -530 MPa, respectively, are both in excess of the maximum stress (-470 MPa) introduced by the CP. Despite the similar peening intensities, the compressive residual stress depths are different: the depth for the SP process extends 100's of microns beneath the surface (~700 μm) whereas the compressive zone for the LP and CP extend to greater depths (~ 1200 μm).
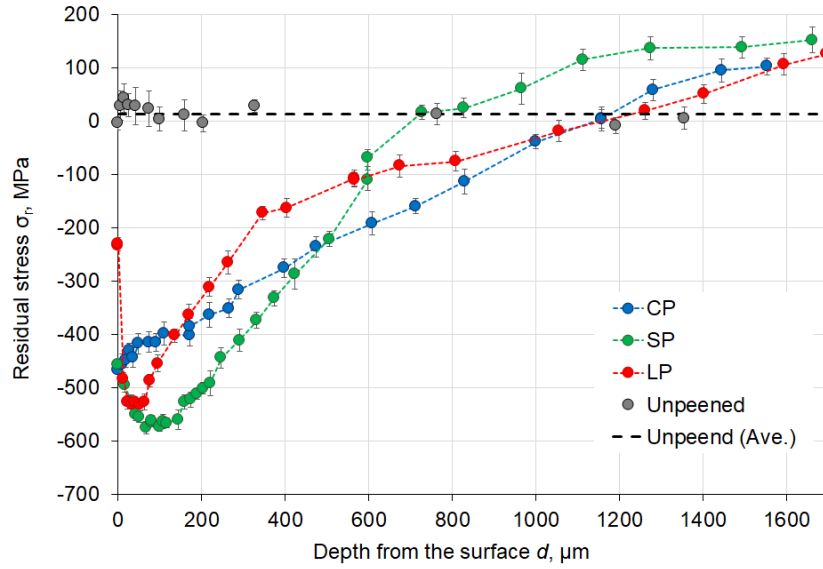
Fig. 2. Comparison of residual stress depth-profiles each specimen measured by X-ray diffraction. The data points represent the average of stresses in the two orthogonal directions. The error bars are estimated from the sin²ψ curves.

The averaged FWHM depth-profiles are summarised in Fig.3. It is well known that diffraction peak broadening is affected by microstructural features, such as dislocation density and crystallite size [46–48]. The FWHM has often been used as a measure of the dislocation density introduced by work hardening caused by local plastic deformation. In common with previous observations, the FWHM is the largest at the surface for all the conditions [33]. Given the different residually stressed depths, it is perhaps surprising that the depth of the increased FWHM is similar for all the surface treatments, suggesting a similar depth of plastic deformation. This suggests significant plasticity to a depth of around 400 μm in each case. A substantially higher level of diffraction peak broadening is introduced by the SP process than the CP and LP processes.

Although the plastic deformation zone appears to extend only to a depth of 400 μm from the surface, tensile residual stresses were recorded by the layer removal method even after removing material to a depth of 1500 μm. This is likely because the residual stresses arising from sample curvature are retained through stress transfer from the material surrounding the crater introduced by the electropolishing method. To confirm this, the surrounding material was removed, and the stresses at 1500 μm depth measured again to clarify the origin of the stresses. After this the residual stresses in the CP, SP, and LP specimens were, −54, 20 and 12 MPa, respectively, indicating that the plastically generated eigenstrain introduced over the first 400 μm is indeed responsible for the whole stress profile.
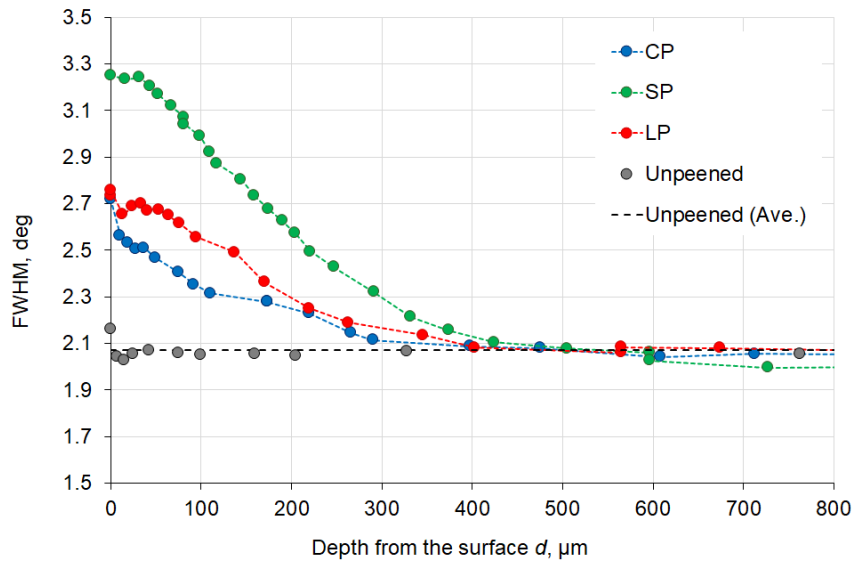
Fig. 3. Diffraction peak FWHM as a function of depth for each surface treatment as determined by X-ray stress measurement.

3.2 Surface morphology

Fig.4 shows the surface topographies of each of the peened samples, observed by laser confocal microscopy, are markedly different.
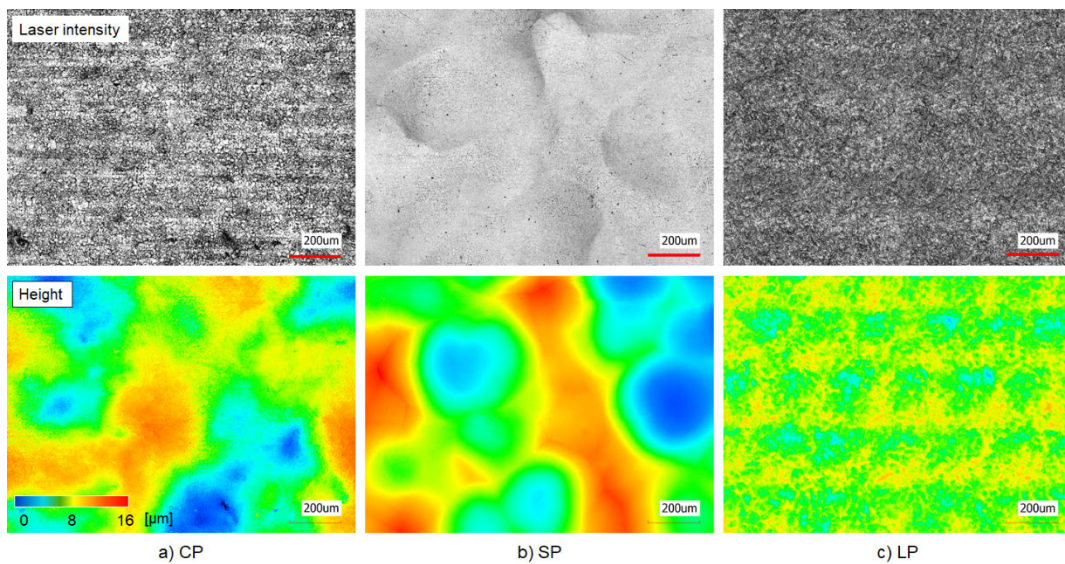

Fig. 4. Surface morphologies after a) CP, b) SP and c) LP treatments observed via laser confocal microscopy showing the laser intensity image (top) with the greyscale indicating the reflected laser intensity at each point and as a height map (bottom), with the colours denoting the sample height.

To facilitate quantitative comparison, height profiles along horizontal lines on across the laser height maps were extracted from Fig.4 and are shown in Fig.5. The height profiles of each specimen exhibit some periodicity. In the case of the CP and SP samples, the periodicity is similar (0.6-1.0 mm peak spacing), although the CP sample displays sharper maxima. By contrast, the LP profile is of lower amplitude having a smaller peak to peak spacing (<0.5 mm) and is generally less smooth. No clear relationship between the surface features and the depth profiles of the residual stress or FWHM was found.
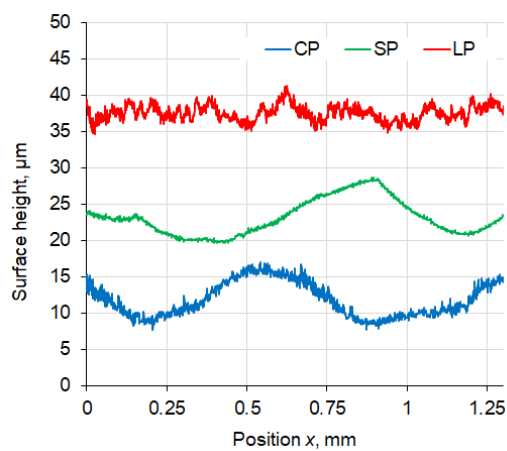

Fig. 5. Surface height profiles along the horizontal direction for each of the surface treatments. The height of each specimen is offset for clarity.

3.3 Hardness depth-profiles

Fig.6 shows the hardness distributions as a function of depth as revealed by nanoindentation testing. Each value was an average of four points at the same depth. In common with the FWHM results, the hardness is higher near-surface and decreases with increasing depth for all treatments. Moreover, the hardness near-surface on the SP and LP specimens is approximately constant over the first 100 μm or so. The hardened zones extend to a depth of around 400 μm, which is the same as the depth-profiles of FWHM.
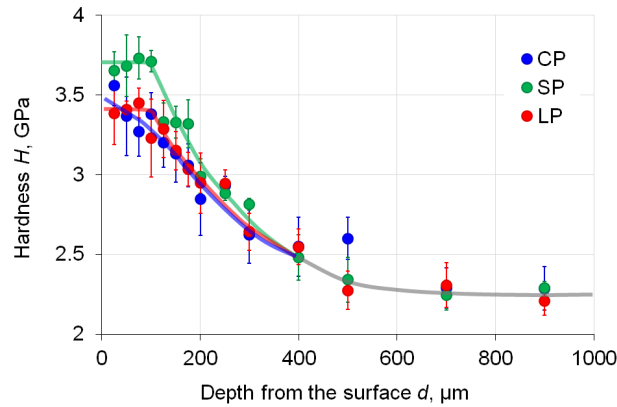
Fig. 6. Variation in nanoindentation hardness against depth from the surface. The continuous lines represent approximate trend lines for clarity.

3.4 EBSD analysis of the near surface microstructures

Representative EBSD maps are shown in Fig.7 for each surface treatment as a function of depth near surface. A small number ($\leqq 1\%$) of unindexed data points were replaced post-acquisition using the standard noise reduction functions in HKL Tango (Oxford Inst.) software. The inverse pole figure (IPF) maps in Fig.7 reveal a similar grain size across the samples. Twins are observed for each treatment; however, the number of twin boundaries is significantly higher for the SP treated specimen and the width of the twins smaller than for the other treatments. It is expected that this high twin density is the result of a large amount of plastic deformation introduced, as shown by the greater broadening of the FWHM. In this context, it is worth remembering that the plastically deformed region extends to a depth of around 400 μm, as evidenced by the FWHM in Fig.3. The amplitude of the grain reference orientation deviation (GROD) angle on the SP specimen is uniformly high over the 80 μm examined (Fig.7 (bottom)). By contrast, for the CP and LP specimens, significant deviations are seen; primarily over the first 40 μm, after which much less deviation is observed. This suggests that although the surface treatment intensities were similar in each case, the inhomogeneous strain distributions and their gradients from the surface differ depending on the processing method.

It is also evident from Fig.7 that the amplitude of GROD near the grain boundaries is significantly larger than that in the grains, especially for the CP and LP treatments. This tendency is similar to the result obtained by polycrystal plasticity finite-element analysis [49] which found that when the strain rate is increased, the plastic deformation near grain boundaries becomes significant. In the CP and LP specimens, the plastic deformation is caused by a shockwave having a strain rate larger than that of the SP and this difference may cause the differences in the microstructure and residual stress depth profiles.
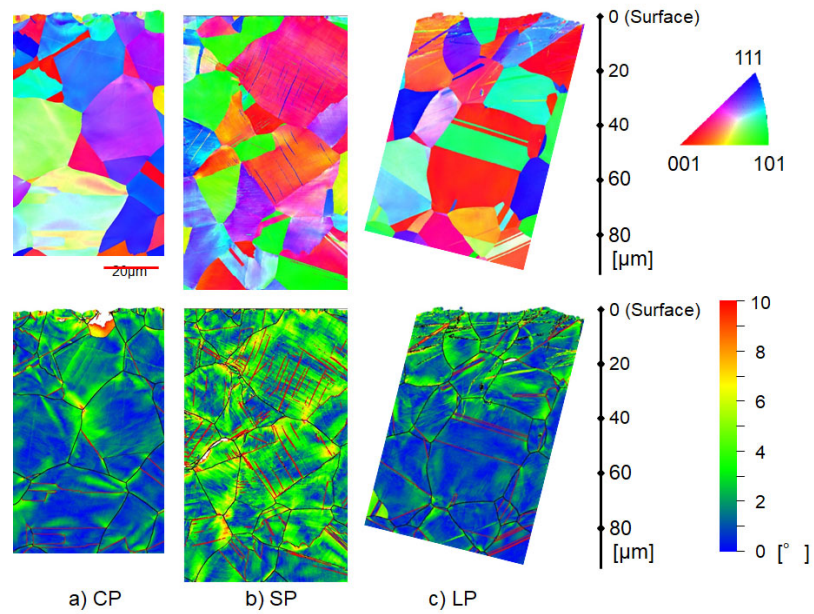
Fig. 7. EBSD analysis for representative cross-section beneath the a) CP, b) SP and c) LP surface treatments showing inverse pole figure maps (top) relative to the normal to the cross-section and grain reference orientation deviation (GROD) maps (bottom). In each case the treated surface is at the top of the figure. Black lines on GROD maps indicate grain boundaries with ~2° (fine) and 2~10° (bold), and red line indicate Σ3 boundaries.

3.5 X-ray diffraction line profile analysis of dislocation structures

X-ray diffraction line profile analysis was performed to infer the number of lattice defects, nature and extent of the dislocation structure and the planar defects, at the surface. Fig.8 shows the diffraction profiles measured for each condition.
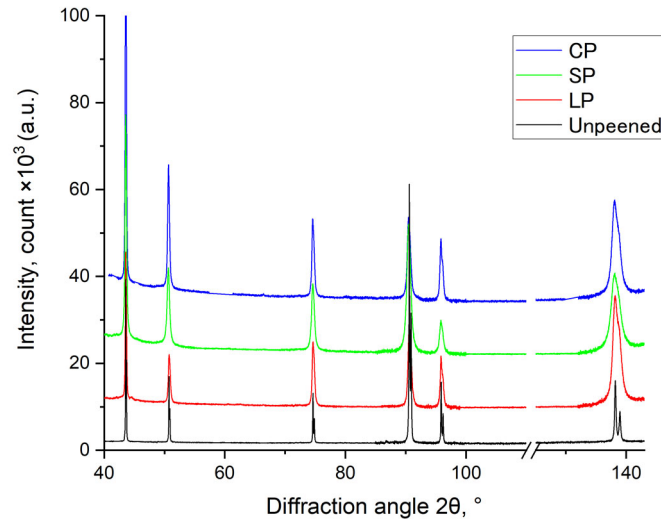
Fig. 8. Whole diffraction profiles (excluding 400 low-intensity reflections) recorded at the surface for the three surface treatments and the untreated reference (profiles offset for clarity).

The results of line profile analysis, dislocation density and plane defect densities, are shown in Fig.9. The CMWP line profile analysis software [41,42] allows only one kind of plane defects to be taken into account at a time. As such, the analysis was performed twice on the assumption of twins and stacking fault defects in turn. An analysis which did not take plane defects into account was also performed leading to three estimates of the dislocation density for each treatment. The inferred dislocation density for the reference specimen is $\sim 1 \times 10^{14}$ m^{-2} in all cases, with very low stacking fault or twin densities. For the surface treatments, the dislocation densities are slightly different depending on the assumed type of defect, but, broadly speaking, the dislocation densities for the CP and LP treated specimens were similar ($\sim 2 \times 10^{15}$ m^{-2}) being about 20x higher than for the untreated case, while that for the SP treatment is approximately 2.5x higher still. Furthermore, the twin and stacking fault probabilities for the SP treatment were 1.1% and 0.7%, respectively, being significantly higher than for the CP and LP specimens. As one might expect, in all cases the dislocation densities inferred by excluding planar defects are higher, because any line broadening due to the planar defects is taken to be due to dislocations (see Fig.9(c)).

In terms of the planar defect density, the characteristics of the LP and CP treated samples are similar, as shown in Fig.9(b). Compared to SP, LP and CP induce significantly fewer planar defects. A similar tendency was also found for the twin boundaries revealed in the EBSD analysis (Fig.7). For each peening type, the number of twin boundaries revealed by EBSD was lower than the value obtained through LPA, but the tendency for more defects in the SP treated sample is clear in both analyses.
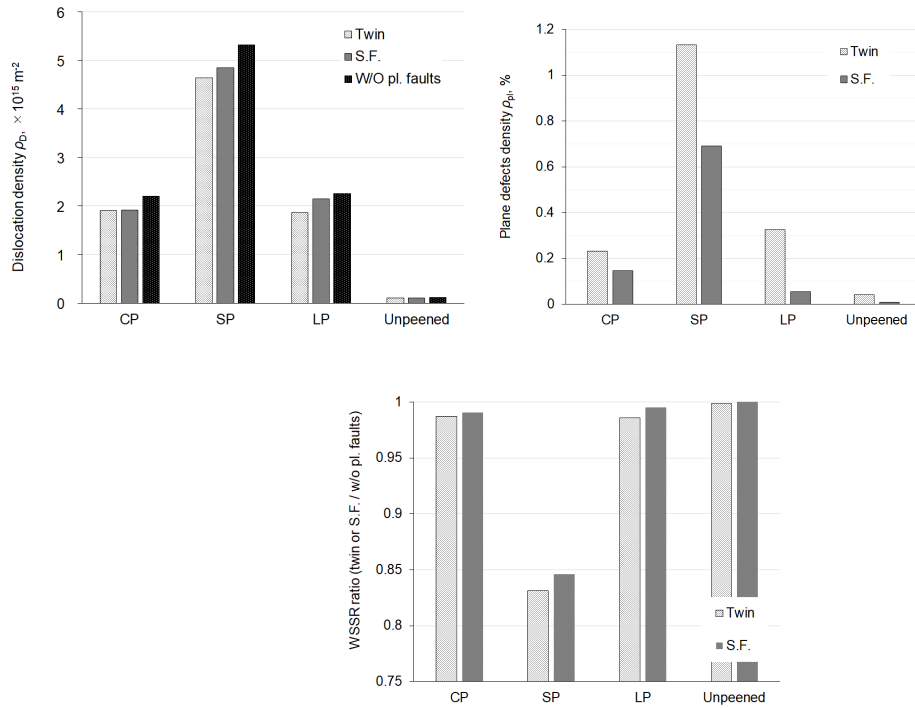
Fig. 9. Lattice defect densities via line profile analysis. a) Dislocation densities, b) density *of twins and stacking faults, and c) weighted sum of squared residuals (WSSRs) ratio for each treatment under several kinds of analysis condition.*

4. Discussion

4.1 Residual stress distributions

It is important to remember that all three treatment levels were chosen to induce similar levels of sample curvature. The compressive residual stress on the CP specimen monotonically decreased with increasing depth. By contrast, the peak compressive stresses in the SP and LP specimens were found to arise subsurface (~50 and 100 μm for the SP and LP respectively). Those peak compressive stresses were larger than the compressive residual stress at the surface of the CP specimen. Furthermore, the compressive residually stressed zone extended to depths around 700 μm in the SP specimen and 1200 μm in the LP and CP specimens. The compressive residual stress is introduced by plastic deformation which is inferred from the FWHM of the diffraction data to decrease with depth from the surface to near to zero at a depth of 400 μm for all three treatments with the plastic deformation much higher for the SP near surface. These three observations, namely higher compressive stress near surface, a shallow compressive stress zone and higher line broadening near the surface are consistent with the fact that to achieve similar specimen curvatures the near-surface stress for the SP must be higher to counterbalance the shallower depth.

Here, bombardment of the sample material during peening generates both tensile and compressive

residual stresses in and around the impression site [50,51]. The stress fields from multiple collisions overlap and result in compressive residual stress on the surface. However, although the residual stress is uniform and compressive at the macro-scale, there are substantial local variations, including tensile regions, at the micron-scale [52]. Hence, the measured compressive residual stress at the surface becomes smaller as it is averaged over the measurement area. Similar phenomena have also been reported in the case of LP when small laser pulses are applied [53]. By contrast, more locally uniform fields are generated when very large square (3 mm) laser pulses are applied [54]. In the case of CP, the compressive residual stress decreased monotonically with increasing depth. This is in part because the large and the small impacts occur at the same time stochastically [55], analogous to multi-stage shot peening using large and small shots. The other reason is that the pressure distribution of an individual cavitation impact is cone-shaped [56].

4.2 Microstructure and hardness

In addition to the residual stress distribution, the impact of different peening methods on the microstructure is of interest. Fig.10 shows the relationship between hardness measured by the nanoindentation test and FWHM of X-ray diffraction line. Although there is some variation, the hardness at a given FWHM is broadly the same regardless of the kind of the peening treatment. This observation enables one to estimate hardness from X-ray diffraction measurement as an easy-to-use approach. Since it is known that the residual stress and yield stress have a great influence on the mechanical performance as mentioned in the introduction [1–4,6], the degree of residual stress and FWHM depth-profiles obtained by X-ray stress measurement are useful in assessing the likely performance of the surface treated materials.
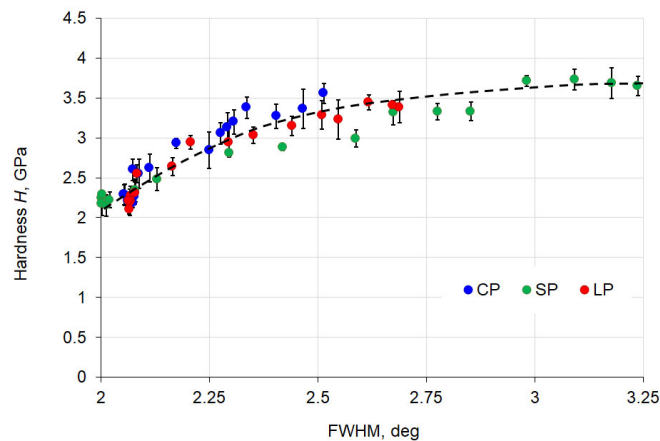

Fig. 10 Relationship between hardness and the FWHM of the X-ray diffraction line. The dashed line is a hand-drawn fit of the relationship.

Here, Vickers hardness was estimated from the nanoindentation hardness. Vickers' hardness, H_V, in

the matrix was 143 ± 3 HV and the ratio of nanoindentation hardness to Vickers hardness at the matrix became 66.7 HV/GPa. The Vickers hardesses were estimated using this value of the ratio and the average nanoindentation hardness at a depth of <75 μm. The estimated hardnesses, of the treated zones, H_V, therefore are 227, 228, 246HV for CP, LP and SP respectively, which is in broad agreement with previous results [35]. Furthermore, hardness values can be converted to an inferred yield stress using the relation $\sigma_Y = H_V \times 9.81 / 3$ [57]. This gives yield stresses of 741, 744, and 804 MPa for the CP, LP, and SP respectively. These estimated yield strengths are significantly higher than the residual stresses introduced. The increase of yield stress is expected to due to increase of dislocation density. In order to the confirm the origin of the strengthening, we estimated the yield stress from the dislocation density using the Bailey–Hirsch relationship, $\sigma_Y = \alpha \rho^{1/2} + \sigma_0$ by the least-square method [58]. Where, α and σ_0 are constants. As the dislocation density, the averaged values in the three analysed results for each specimen (in Fig.9) were used. Fig.11 shows the relationship between the estimated yield stress and the square root of the dislocation density obtained on each specimen. The approximate line represents the relationship between the yield stress and the dislocation density. While there were no significant differences in grain size near the surface in the EBSD analysis, there were differences in the dislocation densities. The increase in hardness depends on the increase in dislocation density regardless of the difference in the peening treatment method, and this can be explained by work hardening arising from an increase in dislocation density.
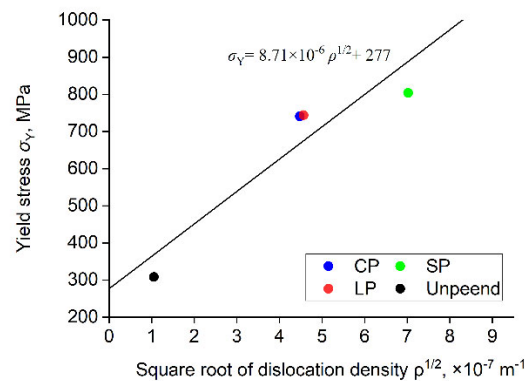

Fig. 11 The relationship between yield stress and square root of dislocation density. the plots for the three specimens (CP, SP, LP) show yield stress estimated from the hardness, and the value of unpeened is the 0.2% proof stress. The line indicates represents a best fit straight line.

5. Conclusions

The residual stresses and microstructural variation, as a function of depth from the surface, have been characterised in austenitic stainless steel treated by shot (SP), cavitation (CP) and laser (LP) peening at similar peening intensities.

1）In the CP treated specimen, the largest compressive residual stress exists at the surface and decreases monotonically with increasing depth from the peened surface, which counterbalance and achieve similar specimen curvatures.

2）The hardness is higher near-surface and decreases with increasing depth for all treatments in common with the FWHM results. The hardness near-surface on the CP and LP are similar while the SP specimen is slightly higher than that of the others. The hardness at a given FWHM is broadly the same regardless of the kind of the peening treatment. This suggests that the depth profile of hardness can be inferred from the FWHM profile.

3）The surface profiles arising from the three different treatments do not appear to be related either to associated residual stress and microstructures.

4）The dislocation density at the surface for the SP specimen is approximately 2.5 times that for the LP and CP specimens. It is also noteworthy that in the case of the SP a large number of twins were observed on the surface by the line profile analysis. The EBSD shows that the extensive work introduced by the SP has generated planar defects near-surface and is consistent with the line broadening analysis in suggesting that the dislocation density is significantly higher for the SP specimen than the LP or CP specimens.

5）The increase in yield stress estimated from the hardness correlates with the increase in dislocation density obtained by the LPA.

Data availability

The raw/processed data required to reproduce these findings cannot be shared at this time due to technical or time limitations.

References

[1]   P. Starker, H. Wohlfahrt, E. Macherauch, Subsurface crack initiation during fatigue as a result of

residual stresses, Fatigue Fract. Eng. Mater. Struct. 1 (1979) 319–327. https://doi.org/10.1111/j.1460-2695.1979.tb00388.x.

[2] Y. Sano, K. Akita, K. Masaki, Y. Ochi, I. Altenberger, B. Scholtes, Laser peening without coating as a surface enhancement technology, J. Laser Micro Nanoeng. 1 (2006) 161–166. https://doi.org/10.2961/jlmn.2006.03.0002.

[3] E. Maawad, Y. Sano, L. Wagner, H.G. Brokmeier, C. Genzel, Investigation of laser shock peening effects on residual stress state and fatigue performance of titanium alloys, Mater. Sci. Eng. A. 536 (2012) 82–91. https://doi.org/10.1016/j.msea.2011.12.072.

[4] H. Soyama, F. Takeo, Comparison between cavitation peening and shot peening for extending the fatigue life of a duralumin plate with a hole, J. Mater. Process. Technol. 227 (2016) 80–87. https://doi.org/10.1016/j.jmatprotec.2015.08.012.

[5] H. Soyama, Y. Okura, The use of various peening methods to improve the fatigue strength of titanium alloy Ti6Al4V manufactured by electron beam melting, AIMS Mater. Sci. 5 (2018) 1000–1015. https://doi.org/10.3934/MATERSCI.2018.5.1000.

[6] R. Strubbia, S. Hereñú, G. Gómez-Rosas, V. Fuster, C. Rubio González, Fatigue Life Improvement in Lean Duplex Stainless Steel by Peening Treatments, Metall. Mater. Trans. A Phys. Metall. Mater. Sci. 50 (2019) 5614–5626. https://doi.org/10.1007/s11661-019-05455-y.

[7] L. Spadaro, S. Hereñú, R. Strubbia, G. Gómez Rosas, R. Bolmaro, C. Rubio González, Effects of laser shock processing and shot peening on 253 MA austenitic stainless steel and their consequences on fatigue properties, Opt. Laser Technol. 122 (2020) 105892. https://doi.org/10.1016/j.optlastec.2019.105892.

[8] Z.D. Wang, G.F. Sun, Y. Lu, M.Z. Chen, K.D. Bi, Z.H. Ni, Microstructural characterization and mechanical behavior of ultrasonic impact peened and laser shock peened AISI 316L stainless steel, Surf. Coatings Technol. 385 (2020) 125403. https://doi.org/10.1016/j.surfcoat.2020.125403.

[9] E.R. de los Rios, A. Walley, M.T. Milan, G. Hammersley, Fatigue crack initiation and propagation on shot-peened surfaces in A316 stainless steel, Int. J. Fatigue. 17 (1995) 493–499. https://doi.org/10.1016/0142-1123(95)00044-T.

[10] Y. Tan, G. Wu, J.M. Yang, T. Pan, Laser shock peening on fatigue crack growth behaviour of aluminium alloy, Fatigue Fract. Eng. Mater. Struct. 27 (2004) 649–656. https://doi.org/10.1111/j.1460-2695.2004.00763.x.

[11] A.G. Sanchez, C. You, M. Leering, D. Glaser, D. Furfari, M.E. Fitzpatrick, J. Wharton, P.A.S. Reed, Effects of laser shock peening on the mechanisms of fatigue short crack initiation and propagation of AA7075-T651, Int. J. Fatigue. 143 (2021) 106025. https://doi.org/10.1016/j.ijfatigue.2020.106025.

[12] D. qiang Tan, J. liang Mo, W. feng He, J. Luo, Q. Zhang, M. hao Zhu, Z. rong Zhou, Suitability of laser shock peening to impact-sliding wear in different system stiffnesses, Surf. Coatings

Technol. 358 (2019) 22–35. https://doi.org/10.1016/j.surfcoat.2018.11.007.

[13]   C. Zhang, M. Zheng, Y. Wang, P. Gao, B. Gan, Effect of high energy shot peening on the wear resistance of TiN films on a TA2 surface, Surf. Coatings Technol. 378 (2019) 124821. https://doi.org/10.1016/j.surfcoat.2019.07.045.

[14]   P. Peyre, X. Scherpereel, L. Berthe, C. Carboni, R. Fabbro, G. Béranger, C. Lemaitre, Surface modifications induced in 316L steel by laser peening and shot-peening. Influence on pitting corrosion resistance, Mater. Sci. Eng. A. 280 (2000) 294–302. https://doi.org/10.1016/S0921-5093(99)00698-X.

[15]   U. Zupanc, J. Grum, Effect of pitting corrosion on fatigue performance of shot-peened aluminium alloy 7075-T651, J. Mater. Process. Technol. 210 (2010) 1197–1202. https://doi.org/10.1016/j.jmatprotec.2010.03.004.

[16]   Y. Sano, M. Obata, T. Kubo, N. Mukai, M. Yoda, K. Masaki, Y. Ochi, Retardation of crack initiation and growth in austenitic stainless steels by laser peening without protective coating, Mater. Sci. Eng. A. 417 (2006) 334–340. https://doi.org/10.1016/j.msea.2005.11.017.

[17]   J.Z. Lu, K.Y. Luo, D.K. Yang, X.N. Cheng, J.L. Hu, F.Z. Dai, H. Qi, L. Zhang, J.S. Zhong, Q.W. Wang, Y.K. Zhang, Effects of laser peening on stress corrosion cracking (SCC) of ANSI 304 austenitic stainless steel, Corros. Sci. 60 (2012) 145–152. https://doi.org/10.1016/j.corsci.2012.03.044.

[18]   D. Karthik, S. Swaroop, Laser shock peening enhanced corrosion properties in a nickel based Inconel 600 superalloy, J. Alloys Compd. 694 (2017) 1309–1319. https://doi.org/10.1016/j.jallcom.2016.10.093.

[19]   M. Kobayashi, T. Matsui, Y. Murakami, Mechanism of creation of compressive residual stress by shot peening, Int. J. Fatigue. 20 (1998) 351–357. https://doi.org/10.1016/S0142-1123(98)00002-4.

[20]   M. Moriyama, T. Naganno, N. Kawagoshi, S. Takaki, E. Nagashima, Effects of Shot Peening on Fatigue Strength of 18%Ni Maraging Steel., Trans. Japan Soc. Mech. Eng. Ser. A. 65 (1999) 2267–2273. https://doi.org/10.1299/kikaia.65.2267.

[21]   A. Evans, S. Kim, J. Shackleton, G. Bruno, M. Preuss, P. Withers, Relaxation of residual stress in shot peened Udimet 720Li under high temperature isothermal fatigue, Int. J. Fatigue. 27 (2005) 1530–1534. https://doi.org/10.1016/j.ijfatigue.2005.07.027.

[22]   H. Mano, S. Kondo, A. Matsumuro, Microstructured Surface Layer Induced by Shot Peening and Its Effect on Fatigue Strength, J. Japan Inst. Met. 70 (2006) 415–419. https://doi.org/10.2320/jinstmet.70.415.

[23]   B.J. Foss, S. Gray, M.C. Hardy, S. Stekovic, D.S. Mcphail, B.A. Shollock, Analysis of shot-peening and residual stress relaxation in the nickel-based superalloy RR1000, Acta Mater. 61 (2013) 2548–2559. https://doi.org/10.1016/j.actamat.2013.01.031.

[24]   S. Bagherifard, S. Slawik, I. Fernández-Pariente, C. Pauly, F. Mücklich, M. Guagliano, Nanoscale surface modification of AISI 316L stainless steel by severe shot peening, Mater. Des. 102 (2016) 68–77. https://doi.org/10.1016/j.matdes.2016.03.162.

[25]   M. Kumagai, K. Kimura, N. Shimada, M. Ishiwata, Inhomogeneous strain and recrystallisation of a shot-peened Inconel 625 alloy after annealing, Mater. Sci. Technol. 35 (2019) 1856–1863. https://doi.org/10.1080/02670836.2019.1651475.

[26]   R. Fabbro, J. Fournier, P. Ballard, D. Devaux, J. Virmont, Physical study of laser-produced plasma in confined geometry, J. Appl. Phys. 68 (1990) 775–784. https://doi.org/10.1063/1.346783.

[27]   P. Peyre, R. Fabbro, Laser shock processing: a review of the physics and applications, Opt. Quantum Electron. 27 (1995) 1213–1229. https://doi.org/10.1007/BF00326477.

[28]   Y. Sano, N. Mukai, K. Okazaki, M. Obata, Residual stress improvement in metal surface by underwater laser irradiation, Nucl. Instruments Methods Phys. Res. Sect. B Beam Interact. with Mater. Atoms. 121 (1997) 432–436. https://doi.org/10.1016/S0168-583X(96)00551-4.

[29]   O. Takakuwa, Y. Kawaragi, H. Soyama, Estimation of the Yield Stress of Stainless Steel from the Vickers Hardness Taking Account of the Residual Stress, J. Surf. Eng. Mater. Adv. Technol. 03 (2013) 262–268. https://doi.org/10.4236/jsemat.2013.34035.

[30]   H. Soyama, Y. Yamauchi, T. Ikohagi, R. Oba, K. Sato, T. Shindo, Marked peening effects by highspeed submerged-water-jets-residual stress change on SUS304, Jet Flow Eng. 13 (1996) 25–32.

[31]   A. King, A.D. Evans, M. Preuss, P.J. Withers, C. Woodward, Study of Residual Stresses Introduced by Laser Shock Peening in Wide Chord Fan Blades by Neutron and Synchrotron Diffraction, J. Neutron Res. 12 (2004) 207–211. https://doi.org/10.1080/10238160410001734694.

[32]   A. King, A. Steuwer, C. Woodward, P.J. Withers, Effects of fatigue and fretting on residual stresses introduced by laser shock peening, Mater. Sci. Eng. A. 435–436 (2006) 12–18. https://doi.org/10.1016/j.msea.2006.07.020.

[33]   M. Turski, S. Clitheroe, A.D. Evans, C. Rodopoulos, D.J. Hughes, P.J. Withers, Engineering the residual stress state and microstructure of stainless steel with mechanical surface treatments, Appl. Phys. A Mater. Sci. Process. 99 (2010) 549–556. https://doi.org/10.1007/s00339-010-5672-6.

[34]   M. Kumagai, K. Akita, M. Imafuku, S. Ohya, X-Ray Line Profile Study on Shot/Laser-Peened Stainless Steel, Adv. Mater. Res. 996 (2014) 39–44. https://doi.org/10.4028/www.scientific.net/AMR.996.39.

[35]   H. Soyama, Comparison between the improvements made to the fatigue strength of stainless steel by cavitation peening, water jet peening, shot peening and laser peening, J. Mater. Process. Technol. 269 (2019) 65–78. https://doi.org/10.1016/j.jmatprotec.2019.01.030.

[36] H. Soyama, Key Factors and Applications of Cavitation Peening, Int. J. Peen. Sci. Technol. 1 (2017) 3–60.

[37] A. Naito, O. Takakuwa, H. Soyama, Development of peening technique using recirculating shot accelerated by water jet, Mater. Sci. Technol. 28 (2012) 234–239. https://doi.org/10.1179/1743284711Y.0000000027.

[38] Y. Sano, K. Akita, T. Sano, A mechanism for inducing compressive residual stresses on a surface by laser peening without coating, Metals (Basel). 10 (2020) 1–12. https://doi.org/10.3390/met10060816.

[39] P. Withers, H.K.D.H. Bhadeshia, Residual stress. Part 1 – Measurement techniques, Mater. Sci. Technol. 17 (2001) 355–365. https://doi.org/10.1179/026708301101509980.

[40] JSMS Committee on X-ray Study of Mechanical Behavior of Materials, Standard for X-Ray Stress Measurement - Iron and Steel -, Society of Materials Science, Japan, 2002.

[41] G. Ribárik, Modeling of diffraction patterns based on microstructural properties, Eötvös Loránd University, 2008.

[42] G. Ribárik, B. Jóni, T. Ungár, Global optimum of microstructure parameters in the CMWP line-profile-analysis method by combining Marquardt-Levenberg and Monte-Carlo procedures, J. Mater. Sci. Technol. 35 (2019) 1508–1514. https://doi.org/10.1016/j.jmst.2019.01.014.

[43] W.B. Pearson, A handbook of lattice spacings and structures of metals and alloys volume 2, Pergamon Press Ltd., London, 1967.

[44] A. Borbély, J. Dragomir-Cernatescu, G. Ribárik, T. Ungár, Computer program ANIZC for the calculation of diffraction contrast factors of dislocations in elastically anisotropic cubic, hexagonal and trigonal crystals, J. Appl. Crystallogr. 36 (2003) 160–162. https://doi.org/10.1107/S0021889802021581.

[45] H.M. Ledbetter, Predicted single-crystal elastic constants of stainless-steel 316, Br. J. Non-Destructive Test. 23 (1981) 286–287.

[46] W.H. Hall, X-Ray Line Broadening in Metals, Proc. Phys. Soc. Sect. A. 62 (1949) 741–743. https://doi.org/10.1088/0370-1298/62/11/110.

[47] B.E. Warren, B.L. Averbach, The Effect of Cold-Work Distortion on X-Ray Patterns, J. Appl. Phys. 21 (1950) 595. https://doi.org/10.1063/1.1699713.

[48] G.K. Williamson, R.E. Smallman, III. Dislocation densities in some annealed and cold-worked metals from measurements on the X-ray Debye-Scherrer spectrum, Philos. Mag. 1 (1956) 34–46. https://doi.org/10.1080/14786435608238074.

[49] S. Kanou, M. Nishikawa, H. Soyama, Analysis of the formation of plastic deformation layer on the surface of polycrystalline metals subjected to a micro-size high-rate shot impact, Int. J. Mech. Sci. 75 (2013) 316–323. https://doi.org/10.1016/j.ijmecsci.2013.07.014.

[50] H. Konishi, Y. Murakami, M. Kobayashi, T. Matsui, Mechanism of Creation of Compressive

Residual Stress by Shot Peening and Its Effect on Fatigue Strength: Analysis of Residual Stress Produced by a Single Shot., Trans. Japan Soc. Mech. Eng. Ser. A. 66 (2000) 1847–1854. https://doi.org/10.1299/kikaia.66.1847.

[51]   S. Yasukawa, S. Ohya, M. Kumagai, T. Kikuchi, Microscopic Residual Stress Distribution Measurement on the Single Dent Surface Assuming Shot Peening (in Japanese), J. Soc. Mater. Sci. Japan. 67 (2018) 375–382. https://doi.org/10.2472/jsms.67.375.

[52]   S. Yasukawa, S. Ohya, K. Tango, K. Takeda, A. Tange, Microscopic Residual Stress Distribution Measurement on the Surface of Shot Peening, J. Soc. Mater. Sci. Japan. 63 (2014) 655–661. https://doi.org/10.2472/jsms.63.655.

[53]   H. Tanaka, K. Akita, Y. Sano, Experimental Study on Compressive Residual Stress Evolution by Pulse Laser Irradiation, J. Soc. Mater. Sci. Japan. 55 (2006) 641–646. http://cat.inist.fr/?aModele=afficheN&cpsidt=18064491.

[54]   A. Evans, G. Johnson, A. King, P.J. Withers, Characterization of laser peening residual stresses in Al 7075 by synchrotron diffraction and the contour method, J. Neutron Res. 15 (2007) 147–154. https://doi.org/10.1080/10238160701372653.

[55]   H. Soyama, A. Lichtarowicz, T. Momma, E.J. Williams, A New Calibration Method for Dynamically Loaded Transducers and Its Application to Cavitation Impact Measurement, J. Fluids Eng. 120 (1998) 712–718. https://doi.org/10.1115/1.2820728.

[56]   H. Soyama, Introduction of compressive residual stress using a cavitating jet in air, J. Eng. Mater. Technol. Trans. ASME. 126 (2004) 123–128. https://doi.org/10.1115/1.1631434.

[57]   J.R. Cahoon, W.H. Broughton, A.R. Kutzak, The determination of yield strength from hardness measurements, Metall. Trans. 2 (1971) 1979–1983. https://doi.org/10.1007/BF02913433.

[58]   J.E. Bailey, P.B. Hirsch, The dislocation distribution, flow stress, and stored energy in cold-worked polycrystalline silver, Philos. Mag. 5 (1960) 485–497. https://doi.org/10.1080/14786436008238300.